Atomic Scale Study on Growth and Heteroepitaxy of ZnO Monolayer on Graphene

Hyo-Ki Hong,[†,¶] Junhyeon Jo,[†,¶] Daeyeon Hwang,[‡] Jongyeong Lee,[†] Na Yeon Kim,[†,§] Seungwoo Son,[†] Jung Hwa Kim,[†] Mi-Jin Jin,[†] Young Chul Jun,[†] Rolf Erni,[‖] Sang Kyu Kwak,[‡,§] Jung-Woo Yoo,[†,⊥] and Zonghoon Lee*[†,§,⊥]

[†]School of Materials Science and Engineering, Ulsan National Institute of Science and Technology (UNIST), Ulsan 44919, Republic of Korea

[‡]School of Energy and Chemical Engineering, Ulsan National Institute of Science and Technology (UNIST), Ulsan 44919, Republic of Korea

[§]Center for Multidimensional Carbon Materials, Institute for Basic Science (IBS), Ulsan 44919, Republic of Korea

[‖]Electron Microscopy Center, Empa — Swiss Federal Laboratories for Materials Science and Technology, CH-8600 Dübendorf, Switzerland

[⊥]Low Dimensional Carbon Material Center, Ulsan National Institute of Science and Technology (UNIST), Ulsan 44919, Republic of Korea

S *Supporting Information*

ABSTRACT: Atomically thin semiconducting oxide on graphene carries a unique combination of wide band gap, high charge carrier mobility, and optical transparency, which can be widely applied for optoelectronics. However, study on the epitaxial formation and properties of oxide monolayer on graphene remains unexplored due to hydrophobic graphene surface and limits of conventional bulk deposition technique. Here, we report atomic scale study of heteroepitaxial growth and relationship of a single-atom-thick ZnO layer on graphene using atomic layer deposition. We demonstrate atom-by-atom growth of zinc and oxygen at the preferential zigzag edge of a ZnO monolayer on graphene through *in situ* observation. We experimentally determine that the thinnest ZnO monolayer has a wide band gap (up to 4.0 eV), due to quantum confinement and graphene-like structure, and high optical transparency. This study can lead to a new class of atomically thin two-dimensional heterostructures of semiconducting oxides formed by highly controlled epitaxial growth.

KEYWORDS: Heteroepitaxy, atomically thin, 2D materials, quantum confinement effect, ZnO monolayer, graphene
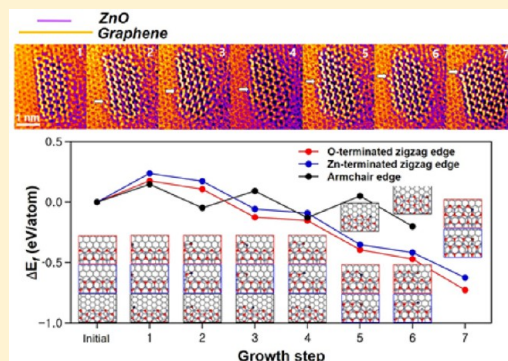
Heteroepitaxy of metal oxide semiconductors on two-dimensional (2D) layered nanomaterials, combining wide band gap and high charge carrier mobility, has become a new integration method for fabricating flexible[1−3] electronic and optoelectronic devices.

Among semiconductor oxides, zinc oxide (ZnO) has been used in novel transparent electronic devices[4−7] as forms of epitaxial layer on graphene. Thermodynamically, hexagonal wurtzite ZnO[5] is the most stable and common form. The wurtzite structure of ZnO can be transformed to a planar[8−10] ZnO monolayer in which Zn and O atoms reside in a trigonal planar coordination, instead of the bulk tetrahedral configuration formed when ZnO is thinned down to a few atomic layers. Since ZnO monolayers on graphene can have many applications in switching electronics and photoactive devices, growth of thin ZnO layers on graphene has been studied extensively.[11−13]

Various deposition techniques, including metal−organic vapor phase epitaxy,[14] as well as hydrothermal[15,16] and electrochemical deposition,[17−19] have been employed for the heteroepitaxial growth of ZnO semiconductors on graphene. However, the strongly hydrophobic graphene limits metal oxide deposition and the wide application of this attractive combination.

Here, we provide experimental evidence for the epitaxial growth of a ZnO monolayer on graphene using atomic resolution transmission electron microscopy (ARTEM) along with the corresponding image simulations and first-principles calculations. Furthermore, we demonstrate through *in situ* observation the atom-by-atom growth of zinc and oxygen at the zigzag edge of the ZnO monolayer on graphene at the atomic scale. We also confirm the heteroepitaxial growth and misorientation angles of this ZnO monolayer by direct
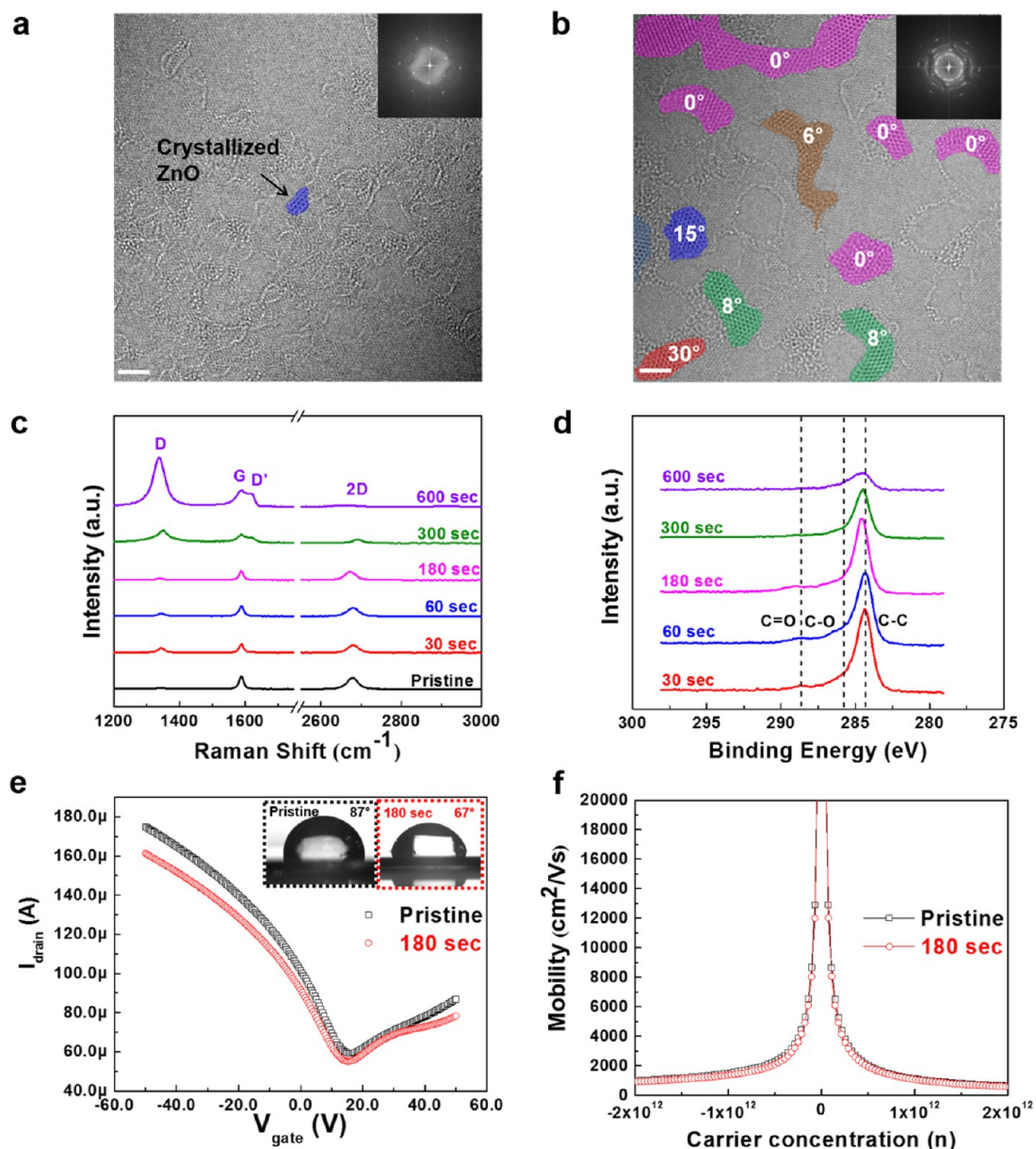
Figure 1. ZnO monolayer on pristine and UV/ozone-treated graphene. (a) Atomic resolution image of ZnO nanoclusters on pristine graphene. The inset in the upper right corner shows the Fourier transform of the image. (b) Atomic resolution image of ZnO nucleation on a graphene substrate after 180 s of UV/ozone treatment. The inset in the upper right corner shows the Fourier transform of the image. (c) Raman spectra of UV/ozone-treated graphene after different treatment times. (d) XPS spectra of the UV/ozone-treated graphene after different treatment times. (e) Current–gate voltage curves of the graphene for different UV/ozone treatment times. The inset in the upper corner shows the contact angle to the graphene substrate treated to UV/ozone from 0 to 180 s. (f) Mobility-carrier concentration curves of the graphene for varying UV/ozone treatment time. The scale bar is 2 nm.

observation and energy calculations of the heterostructures. In addition, we demonstrate the presence of 2–3 nm quantum dots (QDs) of the epitaxial ZnO monolayer grown by atomic layer deposition (ALD). Unlike conventional bulk ZnO, ZnO QDs have potential applications in nanoscale devices, such as photonic and electronic devices, due to the quantum confinement effect.[20,21] The structural and optical properties of the ZnO monolayer on graphene are studied to exploit the quantum phenomena arising from confinement in QDs.

In particular, a ZnO monolayer can preserve the graphene's intrinsic electronic properties,[22−24] high carrier mobility,[25] and optical transmission.[26] Ultrathin 2D oxide semiconductors on graphene have potential applications in optoelectronic devices,

and a new class of 2D heterostructures may arise through this deposition route.

Graphene is a strongly hydrophobic material, which limits the epitaxial growth of semiconductor oxides and thus hinders their various optoelectronic applications. Previously, we attempted to tailor the surface property of graphene surface from hydrophobic to hydrophilic using several methods including O_2 plasma,[27,28] O_3 treatment,[29,30] UV irradiation,[31,32] surface chemical doping,[33] and electrical field.[34]

In this study, we select the UV/ozone treatment[35−37] because it provides sufficient energy to reform the graphene surface state but does not damage the graphene, and it is a simple method uniformly applicable to large areas.

Figure 1 shows a ZnO monolayer grown on pristine graphene and the UV/ozone-treated graphene after 20 ALD cycles. Figure 1a shows the ZnO deposited on the pristine graphene surface after 20 ALD cycles. Blue indicates the crystallized ZnO monolayer. The inset in Figure 1a shows mostly spot patterns of graphene because there is little crystallized ZnO. Figure 1b, however, shows the larger size of ZnO crystals epitaxially grown on the UV/ozone-treated hydrophilic graphene surface after 20 ALD cycles. The diffraction pattern shown in the inset of Figure 1b displays the mixed spot patterns of crystalline ZnO and graphene. The crystalline ZnO monolayer is clearly visible and the ZnO coverage is much larger on the UV/ozone-treated graphene. The misorientation angle of 0° is the most common. In order to investigate the effect of UV/ozone treatment on graphene, Raman spectra are obtained for the graphene as a function of the UV/ozone treatment time from 0 to 600 s (Figure 1c). After up to 180 s of UV/ozone treatment, pristine graphene bands remain intact. However, after 300 s of the treatment, strong D (1345 cm^{-1}) and D′ (1618 cm^{-1}) bands are observed in the spectra, suggesting the formation of lattice defects. These results indicate that excessive UV/ozone treatment damages the graphene lattice.[35] The X-ray photoelectron spectroscopy (XPS) results (Figure 1d) mainly display a C 1s peak, related to the sp^2 C−C bonds based on the UV/ozone treatment time. The XPS spectra show a gradual decrease in the height and broadening of the sp^2 C−C bonds with increasing UV/ozone treatment time. Such behavior is likely caused by p-type doping induced by the UV/ozone treatment.[35] The results of Raman spectroscopy and XPS indicate that excessive UV/ozone treatment induces significant crystal lattice damages and graphene doping. The effects of UV/ozone treatment on the electrical properties are also investigated through field-effect transistor (FET) measurements. The FET devices are fabricated to have a graphene channel (width = 200 μm, length = 5 μm) between the Au electrodes on the SiO$_2$/Si substrate. The mobility of the three pristine graphene FETs is 1346, 1648, and 1490 cm^2/V·s, which changes to 1281, 1424, and 1361 cm^2/V·s, respectively, after the UV/ozone treatment without remarkable Dirac voltage changes. Thus, the mobility decreases only by about 10%, suggesting that our UV/ozone treatment does not severely deteriorate the graphene structure (Figure 1e,f). The inset in Figure 1e shows the change in the contact angle of water on graphene after the 180s UV/ozone treatment, which is measured with an optical contact angle meter in ambient environment. The contact angle decreases from 87° to 67° for the UV/ozone-treated graphene, indicating enhanced hydrophilicity. Therefore, we find that 180 s is the optimum UV/ozone treatment time for ZnO deposition on a graphene substrate. Under these conditions, the graphene surface shows hydrophilicity without deteriorated electrical properties caused by lattice damage.

The diffusion of monomers is the basic form of mass transport on graphene flat surface.[38,39] For technological purposes, it is often desirable to achieve layer-by-layer or Frank−van der Merwe growth to produce smooth layers. Under thermodynamic equilibrium conditions, the growth mode is determined by the surface energy.[40] The epitaxial growth of ZnO wets the flat graphene surface completely when the surface energy of the ZnO monolayer is lower than that of the graphene surface; in the opposite case, the deposited material forms three-dimensional islands, following the Vollmer−Weber growth mode.[40] Figure 2 shows time-elapsed
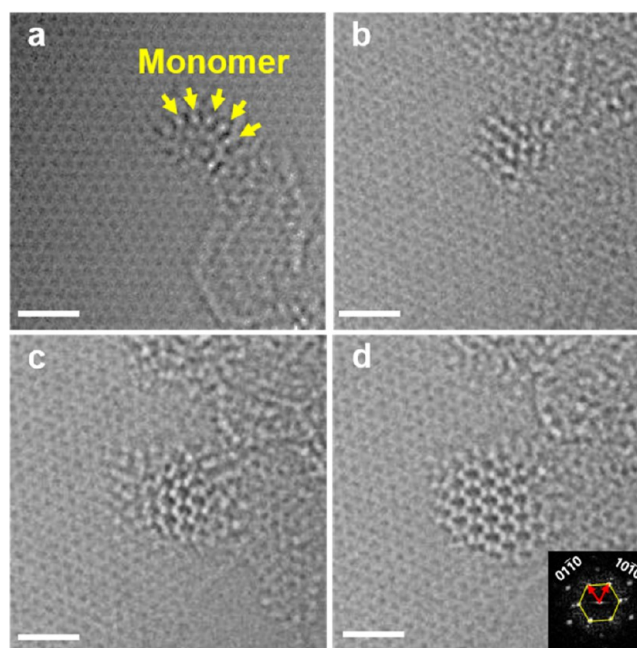

Figure 2. Time-elapsed ARTEM images showing ZnO monolayer growth behavior under electron beam irradiation. (a) ZnO monomer is adsorbed onto the graphene substrate. (b) ZnO becomes amorphous. (c) ZnO forms clusters; unstable clusters are desorbed. (d) The ZnO cluster has periodic atomic arrangement for epitaxial growth on graphene. The scale bar is 1 nm.

ARTEM images taken during the epitaxial growth of the ZnO monolayer on the graphene surface triggered by electron beam irradiation. First, the ZnO monomer is adsorbed onto the graphene's flat surface (Figure 2a). Then, the diffused and desorbed species may also attach to an island nucleated in an earlier growth stage (Figure 2b). The next step is the formation of clusters, where unstable clusters are desorbed (Figure 2c). Then, the ZnO cluster develops which exhibits a periodic atomic arrangement. The epitaxially grown ZnO crystals have a diameter of 2 nm (Figure 2d). Especially, in the lateral growth of ZnO, the highest growth rate is observed along the c-axis and the large facets are usually {10$\bar{1}$0} and {11$\bar{2}$0}, because it is energetically favorable when the [10$\bar{1}$0] or [11$\bar{2}$0] direction of ZnO matches the [10$\bar{1}$0] direction of graphene.[41] The ZnO monolayer has a (0001) polar surface plane, which is atomically flat and stable.[42,43] During the coalescence stage (Supporting Figure 1), there is a distinct difference in the relative orientation of the ZnO crystals and the graphene surface. The ZnO monolayer has a facet edge development as shown in the time-elapsed images. In addition, it has a graphene-like structure along the c-axis and the ZnO adatoms are adsorbed onto the {10$\bar{1}$0} facets. This shows that some crystals in the ZnO monolayer undergo nonepitaxial growth, rotated by 10° during the initial growth stage (Supporting Figure 2).

ZnO is crystallographically misoriented by 30° with respect to the graphene substrate to minimize the dangling bond density. The misorientation angles of 0° and 30° can be explained by the heteroepitaxial relationship between the ZnO monolayer and graphene; it is energetically favorable when the [10$\bar{1}$0] or the [11$\bar{2}$0] crystallographic direction of ZnO matches the [10$\bar{1}$0] direction of the graphene.[41] Figure 3 shows the heteroepitaxial relationship of the ZnO monolayer with the graphene surface, as revealed through ARTEM analysis. Figure 3a shows an atomic resolution image of the
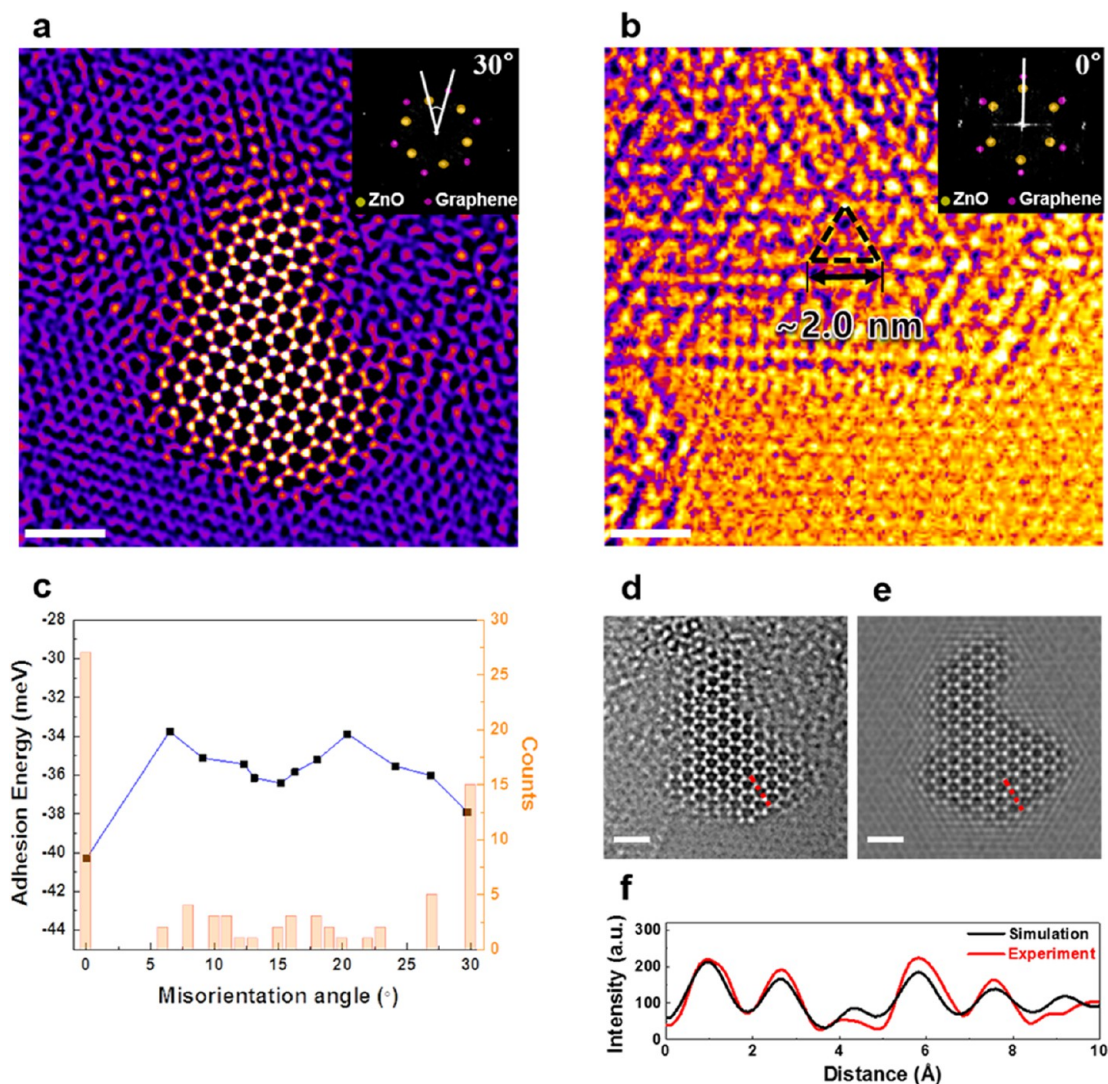
Figure 3. Heteroepitaxial relationship of the ZnO monolayer on graphene analyzed through aberration-corrected TEM. (a) Atomic resolution image of ZnO misoriented by 30° on graphene. The inset in the upper right corner shows the Fourier transform of the image. (b) Atomic resolution image of ZnO misoriented by 0°. The inset in the upper right corner shows the Fourier transform of the image. Triangular moiré patterns are repeatedly observed every 2 nm. (c) Histogram of misorientation angles of ZnO on graphene and adhesion energy of oxygen-terminated triangular ZnO nanocluster on graphene surface vs the misorientation angle. (d) Raw image of part a. (e) Image simulation result of the ZnO monolayer on graphene. (f) Normalized intensity profiles acquired from the image simulation (black line) and experimental image (red line), corresponding to marked profiles in red dashed lines in parts d and e. The scale bars indicate 1 nm.

ZnO monolayer misoriented by 30° on the graphene. The inset in the upper right corner shows the Fourier transform of the image. According to the ARTEM analysis, the atomic model of ZnO/graphene rotated by 30° is simulated as shown in the Supporting Figure 3a. The corresponding simulated diffractogram (Supporting Figure 3a) is in good agreement with the diffractogram of the ARTEM image (Figure 3a). The ZnO monolayer, misoriented by 0° and 30° on the graphene, appears during the initial growth stage and eventually becomes misoriented by 0° as ZnO crystals grow further.

Figure 3b shows an ARTEM image of the ZnO layer on graphene misoriented by 0°. The image clearly shows a unit triangular Moiré pattern with a periodicity of about 2.0 nm, which is attributed to the lattice misfits. The determined lattice constants for ZnO (a ≈ 3.3 Å, c ≈ 5.2 Å) and graphene (a ≈ 2.46 Å) agree well[10,11] with the reported lattice constants of graphene-like ZnO and graphene. These results are in good agreement with the atomic model and the diffractogram

(Supporting Figure 3c,d, respectively). In order to reveal the specific misorientation angles observed through the experiment, the stability of each misorientation angle is assessed by calculating the adhesion energy (E_{ad}) as follows:

$$E_{ad} = (E_{total} - (E_{ZnO} + E_G))/N \qquad (1)$$

where E_{total}, E_{ZnO}, and E_G represent the energies of the ZnO nanocluster on graphene, the freestanding ZnO nanocluster, and the freestanding graphene, respectively, and N is the total number of Zn and O atoms in the ZnO nanoclusters. Based on the density functional theory (DFT) calculations (see DFT calculation in Supporting Information, Note 2) of the different edges of ZnO nanoclusters (Supporting Figure 4 and Model Systems in the Supporting Infomation), the misorientation angles 0° and 30° are more stable for the ZnO monolayer on graphene due to the strong van der Waals interactions between the edge atoms of ZnO and graphene. Figure 3c shows the histogram of the observed misorientation angles and the
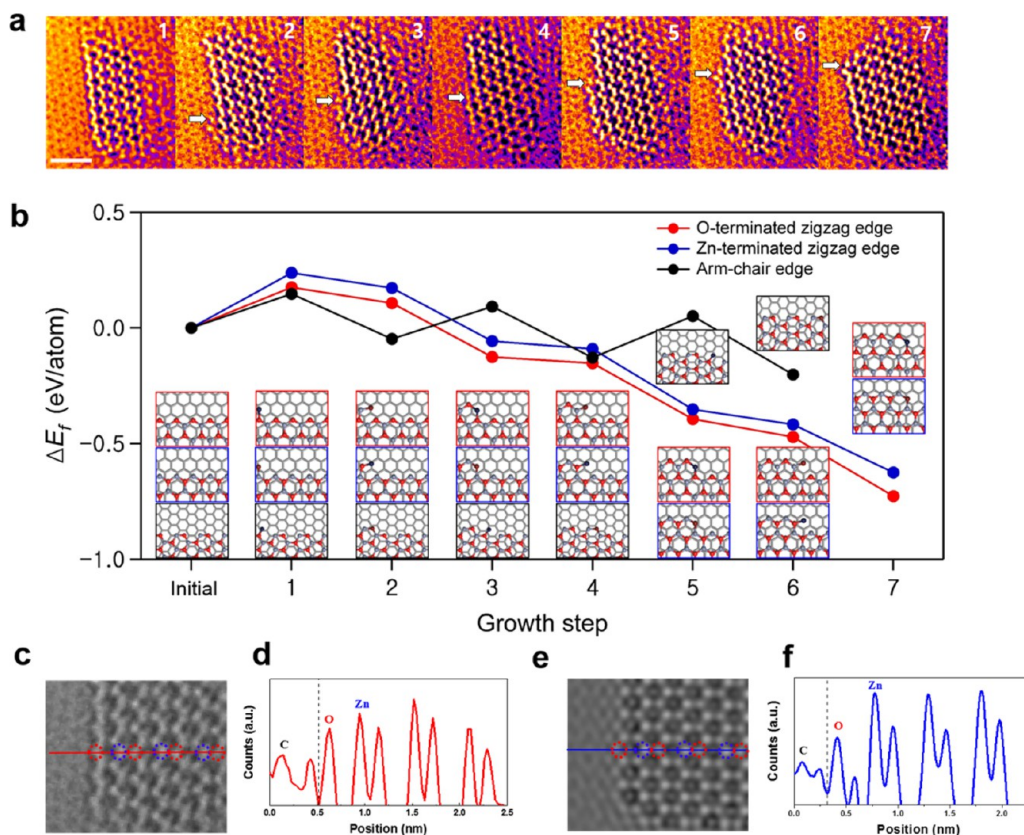
Figure 4. Lateral growth of the ZnO monolayer along the zigzag edges. (a) Time-elapsed ARTEM images show the adsorbed ZnO adatoms on graphene. Additional details can be seen in Movie S1. (b) Relative formation energy (i.e., $\Delta E_f = E_{f\_growth\ step} - E_{f\_initial}$) of the lateral growth of the ZnO monolayer with oxygen- and zinc-terminated zigzag edges and armchair edge. The red and blue spheres represent oxygen and zinc atoms, respectively, and the gray-stick honeycomb network represents graphene. (c) Raw image of part a at final step 7. (d) Intensity profile acquired from the experimental image (red line). (e) Image simulation of part a at final step 7. (f) Intensity profile acquired from the image simulation (blue line). The scale bar is 1 nm.

calculated adhesion energies between the oxygen-terminated triangular ZnO nanocluster and graphene. The counts of the experimental misorientation angle correspond well with the computational adhesion energy.

Figure 3d shows the raw ARTEM image of Figure 3a, and Figure 3e shows the image simulation result of the ZnO monolayer on graphene. It is noteworthy that both images have tiny bright spots in the vacuum regions of the ZnO lattice. The contrast comes from constructive interferences of the exit waves generated by the distance between the ZnO monolayer and the graphene surface. We also compare the variations in the normalized intensity profiles of the experimental image and the simulated image at the imaging condition of the microscope. The similarity of the two intensity profiles in Figure 3d,e confirms the identical atomic structures of ZnO monolayers in these images.

The ZnO monolayer on graphene monolayer assumes a graphene-like structure[8−13] rather than a wurtzite structure. ZnO monolayer nanoclusters have a predominantly zigzag edge configuration with a misorientation angle of 0° on graphene. Here, the *in situ* observation allows for demonstrating the atom-by-atom lateral growth of zinc and oxygen at a zigzag edge of the ZnO monolayer on graphene at atomic scale, as shown in the Supporting Movie 1. Figure 4a, which is a series of snapshots obtained from the movie, shows time-elapsed images of adsorbed ZnO adatoms on a graphene substrate. In order to understand the lateral growth at the edge, the formation energy,

which may reveal the growth path, is estimated through DFT calculation. The formation energy E_f is defined as follows:

$$E_f = (E_{total} - E_G - N_{Zn}E_{Zn} - N_O E_O)/(N_{Zn} + N_O) \quad (2)$$

where E_{total} and E_G represent the energies of the ZnO monolayer on graphene and the freestanding graphene; E_{Zn} and E_O are the energies of zinc and oxygen atoms in vacuum; and N_{Zn} and N_O are the numbers of zinc and oxygen atoms in the total system, respectively. Based on the lateral growth model systems (Supporting Figure 5), the relative formation energy of the ZnO monolayer on graphene is estimated as shown in Figure 4b. After the first unstable adatom absorption, the formation energies tend to decrease. For oxygen- and zinc-terminated zigzag edges, the formation energies gradually decrease as the growth step increases. In particular, a large formation energy drop occurs by stabilizing the ZnO edge when a hexagonal structure is formed by adatom absorption. For the armchair edge, the formation energy fluctuates with increasing growth step. When adatoms form a full hexagonal structure, the formation energy decreases, but when they become dangling atoms, the formation energy increases. Consequently, the lateral growth of ZnO is energetically favorable for the zigzag edge over the armchair edge. In addition, parallel growth is favored less than lateral growth because of the continuous unstable adatom absorption at the pristine edge (Supporting Figure 6).
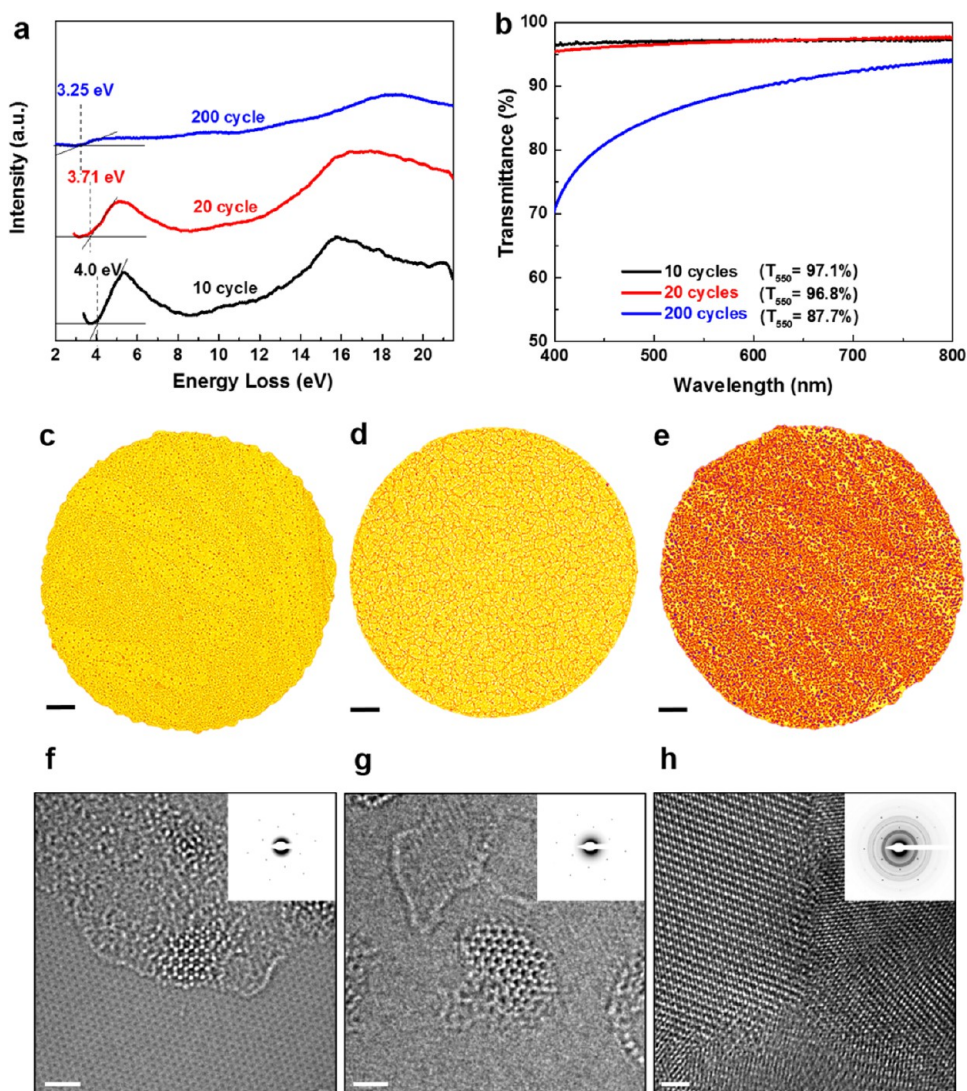
Figure 5. Electronic and optical properties of ZnO deposited with different ALD cycles on UV/ozone treated graphene. (a) STEM-EELS spectra of ZnO deposited with different ALD cycles on UV/ozone-treated graphene. The extrapolation lines (dashed lines) indicate the band gap (E_g) values 4.0, 3.71, and 3.25 eV. Each curve is scaled differently. (b) Optical transmittance measurement of ZnO deposited with different ALD cycles on graphene. (c–e) Bright-field images of suspended UV/ozone-treated graphene after 10, 20, and 200 cycles of ZnO ALD growth. The scale bar is 200 nm. (f–h) ARTEM images of 10, 20, and 200 cycles of ZnO ALD growth on the UV/ozone-treated graphene substrate. The insets in the upper right corner show the electron diffraction patterns of the imaging regions (f–h). The scale bar is 1 nm.

Parts c and e of Figure 4 show the raw ARTEM image of Figure 4a at the final step 7 and the corresponding simulation image at the imaging condition, respectively. The ZnO adatoms are adsorbed onto the oxygen-terminated zigzag edges because these edges are more stable than Zn metal edges (Figure 4b). Figure 4d shows an intensity profile in the raw ARTEM image of Figure 4c, where Zn, O, and C atoms can be distinguished, because the Zn atoms display 4.5% higher intensity than the O atoms with ±1.5% deviation in the real image.[44] This result reveals the lateral growth of ZnO as heteroepitaxy growth on graphene at the atomic scale. The observed ZnO monolayer appears crystallographically identical to the graphene-like structure. We draw attention to two findings from the results: First, the ZnO adatoms at the zigzag edges are energetically favorable, and oxygen-terminated edges are more stable than Zn-terminated edges (Figure 4 and Supporting Figure 5). Second, the ZnO adatoms along the growth direction are

energetically more stable than those parallel to the growth direction (Supporting Figure 6).

Bulk ZnO has a band gap of 3.37 eV at room temperature.[7] However, ZnO monolayer nanoclusters with a diameter of 2–4 nm or smaller (Figure 5f,g) have increased band gaps due to strong quantum confinement effects[20,21] and graphene-like crystallographic structure. Therefore, we anticipate a similar drastic change in the band gap of ZnO monolayer nanoclusters.

In this study, we experimentally measure the band gaps of the ZnO nanoclusters and verify the change in the band gaps of the ZnO monolayer QDs grown on graphene.

Figure 5a shows band gap measurements with electron energy loss spectroscopy (EELS) in the scanning transmission electron microscopy (STEM) mode for ZnO grown on graphene with different ALD cycles. Figure 5a shows the obtained EELS spectra after subtracting zero loss peaks. The band gaps are estimated from these spectra using a power law.[45] The results display higher band gap energy for smaller ZnO

nanoclusters. For instance, a ZnO sample grown with 10 ALD cycles displays a band gap of 4.0 eV, whereas a ZnO sample grown with 200 ALD cycles exhibits a band gap of 3.25 eV, which is close to the bulk ZnO value. The observed gradual spectral shift in the band edge with the ALD cycles can be attributed to the expected quantum confinement effect.[20,21]

We also measure the variation in the band gap energy with a different experimental method. Supporting Figure 8 shows the optical transmission spectra obtained from the UV−vis−NIR spectrophotometer. These spectra can provide plots of $(\alpha h\nu)^2$ as a function of photon energy ($h\nu$) for different ALD cycles— where α is the absorption coefficient of ZnO, defined as follows:[46]

$$\alpha = \left(\frac{1}{\Delta d}\right) \ln\left(\frac{T_1}{T_2}\right) \tag{3}$$

Here, Δd ($= d_2 - d_1$) is the thickness difference between the two ZnO films, and T_1 and T_2 are the transmittances of the two films. If $d_1 = 0$ (and $T_1 = 1$), we can also obtain the absorption coefficient of the ZnO film. The linear fit to the rapidly rising part of a spectrum gives the value for the optical band gap. Similar methods have been used for determining band gaps of various composite films. The ZnO band gaps for 10, 20, and 200 ALD cycles are determined in this way (Supporting Figure 8a−c). Indeed, the obtained band gaps are very close to those measured from the STEM-EELS spectra in Figure 5. This again verifies a significant change in band gap due to the quantum confinement effect in ZnO monolayer nanoclusters on graphene. The ZnO monolayer QDs on 2D materials with their tunable band gap can be a promising template for various photonic and electronic device applications. Figure 5b shows optical transmittance data of ZnO deposited with different ALD cycles on graphene. The ZnO films grown on graphene with 10 and 20 ALD cycles are nearly transparent, with flat optical transmittances of T = 97.1% and 96.8% at 550 nm, respectively. However, ZnO films grown with 200 cycles exhibit substantial reduction in transmittance (T = 87.7% at 550 nm). The drop in optical transmittance is highly nonlinear to the number of ALD cycles[47] because the formation of ZnO nanoclusters, as observed in TEM images, results in a nonlinear expansion of the ZnO deposition area with increasing number of ALD cycles. The morphological development of the ZnO nanoclusters and their epitaxial relationship to graphene are characterized using bright-field TEM and atomic-resolution TEM. Parts c−e of Figure 5 show bright-field TEM images of the ZnO nanostructures grown on graphene after UV/ozone treatment for 180 s with 10, 20, and 200 ALD cycles. These TEM images display orange color for the ZnO monolayer and yellow for the graphene substrate. ZnO coverage on graphene increases significantly with the number of ALD cycles (Figure 5c−e). As shown in Figure 5e, a ZnO monolayer deposited with 200 cycles exhibits highly uniform and high-quality thin films on a large-area graphene substrate. In order to confirm the compositional changes of the 20 and 200 ZnO ALD cycles on UV/ozone-treated graphene, Raman spectroscopy, X-ray diffraction, and X-ray photoelectron spectroscopy (XPS) were carried out. In the Raman spectra of the 200 cycles ZnO on graphene, distinct ZnO peaks were observed near 1131 and 1526 cm^{-1} (Supporting Figure 9). The X-ray diffraction patterns for the 200 cycles ALD grown ZnO on UV/ozone-treated graphene sample revealed $[10\bar{1}0]$, $[0002]$, and $[10\bar{1}1]$ reflections of ZnO (Supporting Figure 10). XPS was also

performed for the 20 and 200 ZnO ALD cycles on UV/ozone-treated graphene on SiO$_2$/Si substrates (Supporting Figure 11). The peak of 1,022 eV in the spectra is corresponding to the Zn−O bonds (Supporting Figure 11a). Also, oxygen 1s spectra at 530.8 eV show O^{2-} ions in the Zn−O bonding of the ZnO film (Supporting Figure 11b). The other peaks located at 532.1 eV correspond to the oxygen atoms bonded to the zinc in the ZnO. We performed STEM HAADF imaging and EELS analysis. The EELS confirmed the presence of Zn and O by the presence of the O K-edge and Zn L-edge of the ZnO monolayer on graphene (Supporting Figure 12). In addition, the compositional analysis of ZnO monolayer was performed using a time-of-flight secondary ion mass spectrometry (TOF-SIMS). The TOF-SIMS maps show ZnO growth areas in yellow. ZnO coverage on graphene was enlarged as the ALD cycles increased (Supporting Figure 14a-c). Parts f−h of Figures 5 show ARTEM images of ZnO nanostructures grown on graphene with 10, 20, and 200 ALD cycles. As shown in Figure 5f, ZnO with 10 ALD cycles starts to develop nanoclusters of 1−2 nm in diameters. The diffraction pattern in the inset of Figure 5f shows mostly spot patterns of graphene because of the insufficient amount of crystalline ZnO. Figure 5g shows that the ZnO monolayer cluster gradually grows in size, by 2−3 nm in diameter. After 200 ALD cycles, coalescence takes place over the entire area of graphene and ZnO nanoclusters merge into larger grains, resulting in the formation of grain boundaries (Figure 5h). The diffraction patterns in the inset of Figure 5h shows the mixed spot patterns of nanosized polycrystalline ZnO and graphene.

In summary, we demonstrate the formation of ZnO monolayer on graphene, which is the thinnest heteroepitaxial layer of semiconducting oxide on monolayer graphene. The optimized UV/ozone treatment enhances the hydrophilicity of the graphene substrate without deteriorating its electrical properties due to lattice damage, and enables the epitaxial growth of ZnO. Through ARTEM investigation, the ZnO monolayer on graphene is directly observed at the atomic scale and its heterostructure is confirmed through image simulation. Most notably, we clearly show the *in situ* atom-by-atom growth of zinc and oxygen at the zigzag edge of the ZnO monolayer on graphene at the atomic scale. Both ARTEM observation and the calculation confirm that oxygen-terminated zigzag edges are more stable than zinc-terminated zigzag and armchair edges. We determine that two dominant misorientation angles (0° and 30°) are associated with the epitaxial growth of the ZnO monolayer on graphene and that the misorientation angle of 0° becomes more prominent as the ZnO monolayer grows. Moreover, we experimentally determine that the monolayer ZnO on graphene has a wide band gap of up to 4.0 eV, which is different from that of other ZnO nanostructures, due to the quantum confinement effect and the crystallographic structure. The heteroepitaxial stack of the thinnest 2D oxide semiconductors on graphene has potential for future optoelectronic device applications associated with high optical transparency and flexibility. This study can lead to a new class of 2D heterostructures including semiconducting oxides formed by highly controlled epitaxial growth through a deposition route.

■ ASSOCIATED CONTENT

⑤ Supporting Information

The Supporting Information is available free of charge on the ACS Publications website at DOI: 10.1021/acs.nanolett.6b03621.

Experimental methods and additional data (PDF)
Supporting Movie 1, showing time-elapsed images of adsorbed ZnO adatoms on a graphene substrate (AVI)

■ AUTHOR INFORMATION

Corresponding Author

*(Z.L.) E-mail: zhlee@unist.ac.kr).

ORCID

Hyo-Ki Hong: 0000-0002-9722-9615
Jung Hwa Kim: 0000-0002-2615-963X
Sang Kyu Kwak: 0000-0002-0332-1534
Jung-Woo Yoo: 0000-0001-7038-4001
Zonghoon Lee: 0000-0003-3246-4072

Author Contributions

¶These authors contributed equally to this work.

Notes

The authors declare no competing financial interest.

■ REFERENCES

(1) Choi, D.; Choi, M. Y.; Choi, W. M.; Shin, H. J.; Park, H. K.; Seo, J. S.; Park, J.; Yoon, S. M.; Chae, S. J.; Lee, Y. H.; Kim, S. W.; Choi, J. Y.; Lee, S. Y.; Kim, J. M. *Adv. Mater.* **2010**, *22*, 2187−2192.

(2) Chung, K.; Lee, C. H.; Yi, G. C. *Science* **2010**, *330*, 655−657.

(3) Lee, C. H.; Kim, Y. J.; Hong, Y. J.; Jeon, S. R.; Bae, S.; Hong, B. H.; Yi, G. C. *Adv. Mater.* **2011**, *23*, 4614−4619.

(4) Carcia, P. F.; McLean, R. S.; Reilly, M. H.; Nunes, G. *Appl. Phys. Lett.* **2003**, *82*, 1117−1119.

(5) Pearton, S. J.; Norton, D. P.; Ip, K.; Heo, Y. W.; Steiner, T. *Superlattices Microstruct.* **2003**, *34*, 3−32.

(6) Nomura, K.; Ohta, H.; Ueda, K.; Kamiya, T.; Hirano, M.; Hosono, H. *Science* **2003**, *300*, 1269−1272.

(7) Wang, Z. L. *J. Phys.: Condens. Matter* **2004**, *16*, R829−R858.

(8) Freeman, C. L.; Claeyssens, F.; Allan, N. L.; Harding, J. H. *Phys. Rev. Lett.* **2006**, *96*, 066102.

(9) Tu, Z. C.; Hu, X. *Phys. Rev. B: Condens. Matter Mater. Phys.* **2006**, *74*, 035434.

(10) Tusche, C.; Meyerheim, H. L.; Kirschner, J. *Phys. Rev. Lett.* **2007**, *99*, 026102.

(11) Quang, H. T.; Bachmatiuk, A.; Dianat, A.; Ortmann, F.; Zhao, J.; Warner, J. H.; Eckert, J.; Cunniberti, G.; Rummeli, M. H. *ACS Nano* **2015**, *9*, 11408−11413.

(12) Lee, J.; Sorescu, D. C.; Deng, X. *J. Phys. Chem. Lett.* **2016**, *7*, 1335−1340.

(13) Demel, J.; Pleštil, J.; Bezdička, P.; Janda, P.; Klementová, M.; Lang, K. *J. Phys. Chem. C* **2011**, *115*, 24702−24706.

(14) Kim, Y. J.; Lee, J. H.; Yi, G. C. *Appl. Phys. Lett.* **2009**, *95*, 213101.

(15) Akhavan, O. *ACS Nano* **2010**, *4*, 4174−4180.

(16) Kim, Y. J.; Hadiyawarman; Yoon, A.; Kim, M.; Yi, G. C.; Liu, C. *Nanotechnology* **2011**, *22*, 245603.

(17) Yin, Z.; Wu, S.; Zhou, X.; Huang, X.; Zhang, Q.; Boey, F.; Zhang, H. *Small* **2010**, *6*, 307−312.

(18) Wu, S. X.; Yin, Z. Y.; He, Q. Y.; Huang, X. A.; Zhou, X. Z.; Zhang, H. *J. Phys. Chem. C* **2010**, *114*, 11816−11821.

(19) Xu, C.; Lee, J.-H.; Lee, J.-C.; Kim, B.-S.; Hwang, S. W.; Whang, D. *CrystEngComm* **2011**, *13*, 6036−6039.

(20) Viswanatha, R.; Sapra, S.; Satpati, B.; Satyam, P. V.; Dev, B. N.; Sarma, D. D. *J. Mater. Chem.* **2004**, *14*, 661−668.

(21) Kukreja, L. M.; Misra, P.; Fallert, J.; Sartor, J.; Kalt, H.; Klingshirn, C. *Ieee* **2008**, 61−66.

(22) Saito, R.; Fujita, M.; Dresselhaus, G.; Dresselhaus, M. S. *Appl. Phys. Lett.* **1992**, *60*, 2204−2206.

(23) Geim, A. K.; Novoselov, K. S. *Nat. Mater.* **2007**, *6*, 183−191.

(24) Castro Neto, A. H.; Guinea, F.; Peres, N. M. R.; Novoselov, K. S.; Geim, A. K. *Rev. Mod. Phys.* **2009**, *81*, 109−162.

(25) Bolotin, K. I.; Sikes, K. J.; Jiang, Z.; Klima, M.; Fudenberg, G.; Hone, J.; Kim, P.; Stormer, H. L. *Solid State Commun.* **2008**, *146*, 351−355.

(26) Wang, F.; Zhang, Y. B.; Tian, C. S.; Girit, C.; Zettl, A.; Crommie, M.; Shen, Y. R. *Science* **2008**, *320*, 206−209.

(27) Gokus, T.; Nair, R. R.; Bonetti, A.; Bohmler, M.; Lombardo, A.; Novoselov, K. S.; Geim, A. K.; Ferrari, A. C.; Hartschuh, A. *ACS Nano* **2009**, *3*, 3963−3968.

(28) Shin, Y. J.; Wang, Y.; Huang, H.; Kalon, G.; Wee, A. T. S.; Shen, Z.; Bhatia, C. S.; Yang, H. *Langmuir* **2010**, *26*, 3798−3802.

(29) Lee, B.; Park, S.-Y.; Kim, H.-C.; Cho, K.; Vogel, E. M.; Kim, M. J.; Wallace, R. M.; Kim, J. *Appl. Phys. Lett.* **2008**, *92*, 203102.

(30) Leconte, N.; Moser, J.; Ordejon, P.; Tao, H. H.; Lherbier, A.; Bachtold, A.; Alsina, F.; Sotomayor Torres, C. M.; Charlier, J. C.; Roche, S. *ACS Nano* **2010**, *4*, 4033−4038.

(31) Liu, L.; Ryu, S. M.; Tomasik, M. R.; Stolyarova, E.; Jung, N.; Hybertsen, M. S.; Steigerwald, M. L.; Brus, L. E.; Flynn, G. W. *Nano Lett.* **2008**, *8*, 1965−1970.

(32) Xu, Z.; Ao, Z.; Chu, D.; Younis, A.; Li, C. M.; Li, S. *Sci. Rep.* **2014**, *4*, 6450.

(33) Liu, H.; Liu, Y.; Zhu, D. *J. Mater. Chem.* **2011**, *21*, 3335−3345.

(34) Jiang, Q. G.; Ao, Z. M.; Chu, D. W.; Jiang, Q. *J. Phys. Chem. C* **2012**, *116*, 19321−19326.

(35) Huh, S.; Park, J.; Kim, Y. S.; Kim, K. S.; Hong, B. H.; Nam, J. M. *ACS Nano* **2011**, *5*, 9799−9806.

(36) Mulyana, Y.; Uenuma, M.; Ishikawa, Y.; Uraoka, Y. *J. Phys. Chem. C* **2014**, *118*, 27372−27381.

(37) Wang, W.; Ruiz, I.; Lee, I.; Zaera, F.; Ozkan, M.; Ozkan, C. S. *Nanoscale* **2015**, *7*, 7045−7050.

(38) Jiang, B.; Zhang, C.; Jin, C.; Wang, H.; Chen, X.; Zhan, H.; Huang, F.; Kang, J. *Cryst. Growth Des.* **2012**, *12*, 2850−2855.

(39) Peng, Z. A.; Peng, X. G. *J. Am. Chem. Soc.* **2002**, *124*, 3343−3353.

(40) Kohler, U.; Dorna, V.; Jensen, C.; Kneppe, M.; Piaszenski, G.; Reshoft, K.; Wolf, C. *Elsevier Science Bv* **2004**, 391−412.

(41) Jo, J.; Yoo, H.; Park, S. I.; Park, J. B.; Yoon, S.; Kim, M.; Yi, G. C. *Adv. Mater.* **2014**, *26*, 2011−2015.

(42) Dulub, O.; Diebold, U.; Kresse, G. *Phys. Rev. Lett.* **2003**, *90*, 016102.

(43) Lauritsen, J. V.; Porsgaard, S.; Rasmussen, M. K.; Jensen, M. C. R.; Bechstein, R.; Meinander, K.; Clausen, B. S.; Helveg, S.; Wahl, R.; Kresse, G.; Besenbacher, F. *ACS Nano* **2011**, *5*, 5987−5994.

(44) Ryu, G. H.; Park, H. J.; Ryou, J.; Park, J.; Lee, J.; Kim, G.; Shin, H. S.; Bielawski, C. W.; Ruoff, R. S.; Hong, S.; Lee, Z. *Nanoscale* **2015**, *7*, 10600−10605.

(45) Rafferty, B.; Brown, L. M. *Phys. Rev. B: Condens. Matter Mater. Phys.* **1998**, *58*, 10326−10337.

(46) Kim, E.; Jiang, Z. T.; No, K. *Jpn. J. Appl. Phys.* **2000**, *39*, 4820−4825.

(47) Kim, K.; Lee, H. B.; Johnson, R. W.; Tanskanen, J. T.; Liu, N.; Kim, M. G.; Pang, C.; Ahn, C.; Bent, S. F.; Bao, Z. *Nat. Commun.* **2014**, *5*, 4781.